

AD-A029 425

RIA-76-U675

AD-A029 425



TECHNICAL
LIBRARY

Report 2174

HYPERVELOCITY-IMPACT SHOCK-INDUCED
DAMAGE TO STEEL ARMOR

April 1976

Approved for public release; distribution unlimited.

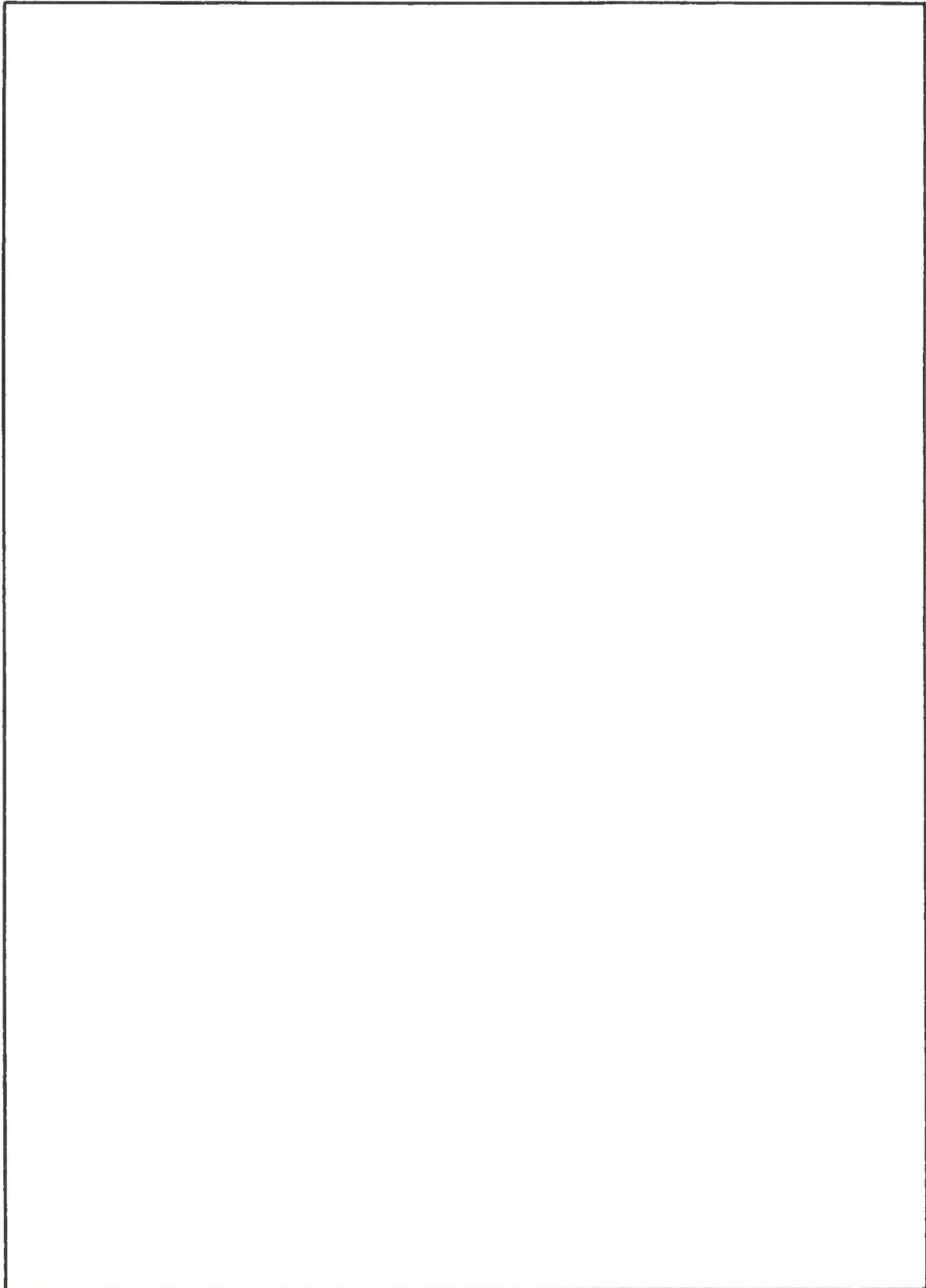


U.S. ARMY MOBILITY EQUIPMENT
RESEARCH AND DEVELOPMENT COMMAND
FORT BELVOIR, VIRGINIA

Destroy this report when it is no longer needed.
Do not return it to the originator.

UNCLASSIFIED

SECURITY CLASSIFICATION OF THIS PAGE(When Data Entered)



UNCLASSIFIED

ii SECURITY CLASSIFICATION OF THIS PAGE(When Data Entered)

CONTENTS

Section	Title	Page
I	INTRODUCTION	1
II	EXPERIMENTAL RESULTS	2
III	DISCUSSION OF EXPERIMENTAL RESULTS	6
IV	2-d COMPUTATIONS	9
V	THE 130-kbar PHASE CHANGE IN MARTENSITIC STEEL	10
VI	INCIPIENT SPALL OR FRACTURE CRITERIA	14
VII	COMPLETE AND BACKFACE SPALL	15
VIII	SUMMARY AND CONCLUSIONS	18

ILLUSTRATIONS

Figure	Title	Page
1	Spallation Damage in 1.25-cm Wrought Steel by Impact of a 0.52-g Nylon Sphere at 5.18 km/s and in 2.53-cm Wrought Steel by Impact of a 0.7-g Steel Sphere at 5.63 km/s	3
2	Phase Change and Associated Damage Below the Crater Resulting from the Impact of an H ₂ O/Lexan Sphere on 2.5-cm Wrought Steel. The Projectile Mass Was 0.32-g and the Impact Velocity was 6.03 km/s	3
3	Spall Layer Formed by a Triangular Pulse	5
4	Spallation Damage in 1.25-cm Wrought Steel by Hollow Lexan Sphere. Mass = 0.565 g; Diameter = 1.08 cm; Impact Velocity = 5.6 km/s	5
5	Phase Diagram of Iron	12
6	Hugoniot States of Iron	12
7	Spall Damage in Homogeneous Wrought Steel Plate	17
8	Backface Bulge (or Spall Layer Thickness) vs. Impact Velocity	17

HYPERVELOCITY-IMPACT SHOCK-INDUCED DAMAGE TO STEEL ARMOR

I. INTRODUCTION

An In-house Laboratory Independent Research (ILIR) program was conducted at the Mobility Equipment Research and Development Command (MERADCOM) to design hypervelocity projectiles that maximize backface spallation in steel armor. The projectiles are small (0.5 to 5 g each) so that several hundred can be located on one end of an explosive driver weighing 15 to 30 kg. The projectiles would be ejected in a near-vertical downward direction toward a target in a shotgun pattern at ejection velocities of 8 to 10 km/s and at a stand-off distance of 20 to 50 m. This enables the consideration of large lethal, or damage, radii of the order of tens of meters. The primary target for the experimental program has been steel armor 2 to 5 cm thick. Damage would be by backface spallation and fragmentation and the resultant effects on personnel, munitions, fuel, equipment, instruments, and soft interior components (of military vehicles) such as cabling.

When the program started two years ago, there was insufficient information on spallation physics to design the type of projectile desired. Accordingly, a program was started to obtain the needed experimental and analytical information. The specific goal was to design a projectile capable of shaping the pulse induced in the steel target in such a way that a large amount of steel would be ejected from the backface of the specimen in the form of many small damaging fragments. During the course of the research, new phenomena were observed and are reported herein. In particular, the importance of the 130-kbar phase change in martensitic steel and the resultant effect on spallation are discussed.

Over 100 successful impact experiments were performed in the Naval Research Laboratory (NRL) light gas-gun facility. The experiments were designed and the results were analyzed at MERADCOM. Metallurgical examination of the impacted specimens was done at the Stanford Research Institute (SRI), with some assistance from Sandia Laboratories Albuquerque (SLA). The 2-d code calculations were done by SLA. Mechanical material properties of the target materials were measured at MERADCOM.

In order to develop reliable theory and associated analytical tools, simple spherical projectiles, mostly weighing less than 1 g, were used. Impact angles were generally normal, although a few non-normal impacts were made. Also, a few impacts were made with both simple and composite non-spherical projectiles. Projectile materials included nylon, lexan, water, heavy oil, steel, and several different ceramics.

These choices of projectile materials were based on the fact that the proposed warhead is weight-limited rather than volume-limited. This enables many projectiles of the same size to be carried, or larger projectiles may be used. Size is important because the projectile diameter should be of the order of, or greater than, the target thickness in order to optimize spall.¹ The vaporization or sublimation energy of the projectile material should be small compared to the kinetic energy of impact. The general idea is to convert most of the impact energy into induced shock. This means that inefficient processes such as penetration should be minimized. Most of the targets were wrought, homogeneous steel plate stock 1.25 cm and 2.5 cm thick. The steel was a carbon manganese-nickel-chromium-molybdenum alloy which was austenitized at 900° C, water quenched, and tempered at 540° C. The representative hardness was 360 Brinell (Bhn), and the approximate quasi-static tensile strength was 12 kbars. The dynamic spall strength corresponded to a critical tensile pressure of 38 kbar.^{2 3 4 5}

After impact, the target specimens were dissected through the crater center, polished, etched, and examined metallurgically by SRI, SLA, and MERADCOM. Extensive 2-d code calculations of the impact spall phenomena for one specimen were made by SLA. SLA also measured spall strength and equation of state.

The experimental results are summarized in Section II. They are analyzed and discussed in Section III. The 2-d computations performed by SLA are described in Section IV. The 130-kbar phase change and spall phenomena are discussed in the remaining sections.

II. EXPERIMENTAL RESULTS

A photograph of a dissected impact crater is shown in Figure 1a. The target material was 1.25-cm-thick wrought steel. The projectile was a 0.52-g nylon sphere with a diameter of 0.95 cm and an impact velocity of 5.18 km/s. The crater is representative of craters formed by impact of lexan-encased H₂O and solid nylon spheres. The walls of such craters exhibit a series of evenly spaced ridges, or serrations, which are symmetric about a central axis of rotation. The macrocracks observed extend downward from the bottom of the valleys in the crater floor. In the case of steel-on-steel impacts (Figure 1b), the serrations in the craters are not observed and the macro-

¹ There is some experimental evidence that much smaller (non-penetrating) projectiles are efficient spallators. (A spallator is a projectile that optimizes backface spall. A penetrator optimizes penetration.)

² J. W. Bond and G. W. Ullrich, "Two-Dimensional Spallation induced by Hypervelocity Impact in Wrought Steel Plate," USAMERDC Report 1067, July 1973.

³ A. Stevens, Personal Communication, SLA, 1973.

⁴ D. A. Shockey, "Support of Armor Fragmentation Studies," SRI Project PYU 2151, 15 October 1973.

⁵ D. A. Shockey, "Hypervelocity Impact and Associated Phenomena," SRI Project PYU 2151, 18 December 1973.



Figure 1. Spallation damage in (a) 1.25-cm wrought steel by impact of a 0.52-g nylon sphere at 5.18 km/s and in (b) 2.53-cm wrought steel by impact of a 0.7-g steel sphere at 5.63 km/s.

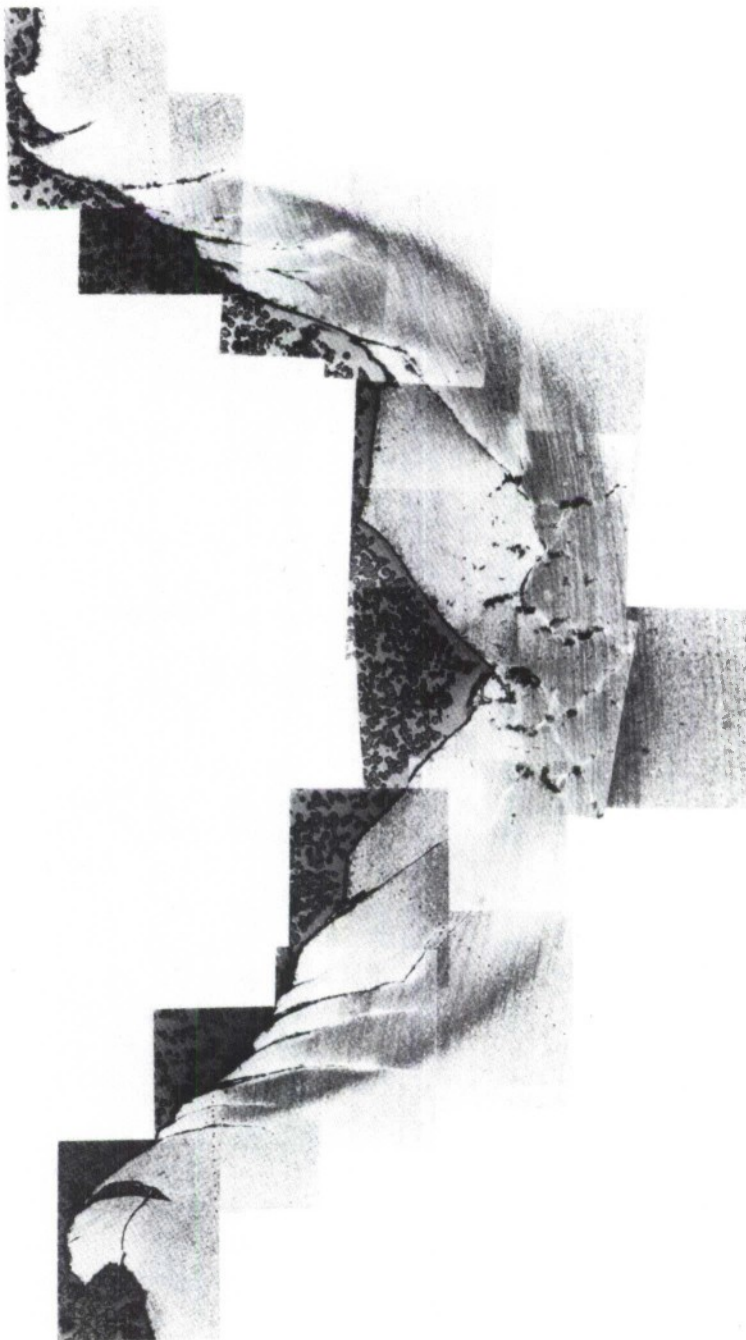


Figure 2. Phase change and associated damage below the crater resulting from the impact of an H₂O/Lexan sphere on 2.5-cm wrought steel. The projectile mass was 0.32 g and the impact velocity was 6.03 km/s.

cracks extend upward. (This difference has not been explained.) Figure 2 shows a 10X photograph of the bottom of the center of a crater produced by a 6.03-km/sec impact of a 0.35-g H₂O/Lexan sphere on a 2.5-cm wrought steel target. The apparent shaded region extends completely around the crater and is readily visible on almost all of the impact specimens. This region has extremely high hardness (500 Bhn) and displays a fine, untempered, martensitic microstructure. This observed metallurgical transformation has been shown to be due to the 130-kbar polymorphic phase transition in iron or martensitic steel.^{6 7} The fine adiabatic shear lines are readily observable on this photograph; also, note the large voids below the bottom of the crater.

When the stress wave, induced at impact, travels through the target and reflects in tension from the backface, a spall layer, or gap, is produced (as seen in Figure 1). Spall is not observed for these conditions at velocities below about 3 km/s. At slightly greater velocities, incipient spall is observed by the appearance of microcracks. The microcracks coalesce to form a complete spall layer at about 3.1 km/s. As the impact velocity is increased, the width and diameter of the spall layer also increase, and at some higher velocity the backface plugs or fragments. Non-adiabatic shear occurs at the outer edge of the spall layer. For a 0.52-g nylon sphere on 1.25-cm wrought steel, backface plugging occurs at about 5.8 km/s. For smaller (lighter) spheres, or for thicker targets, the plugging (or backface fragmenting) velocity is higher.

In spite of the extensive experimentation just described (as well as all other experimentation performed in the U.S.), it is still not possible to design an effective spallator. A few preliminary guidelines have been obtained, however. These are complicated, hence there is insufficient space in this report to present details. Briefly, it is clear that pulse shaping is the key to the production of damaging backface spall. This is exemplified in Figure 3 which shows the reflection and resultant spall of a triangular stress pulse. The incident pulse reflects in tension at the free surface x_0 . When the spall threshold is exceeded, a spall layer is formed at x_1 . The distance $x_1 - x_0$ must be sufficiently small so that the backface can be spalled and fragmented but sufficiently large so that a damaging amount of backface material is ejected.

After the spall layer is formed at x_1 , the subsequent stress pulse reflects at x_1 rather than at x_0 . This can result in the formation of a second spall layer at x_2 . Obviously, this sequence of events can be repeated to form multiple spall layers. In order to prove this hypothesis, several different projectile configurations were tested. One of these configurations was a hollow plastic sphere. The reasoning here was that upon impact more mass would be delivered at the impact periphery and "double-impact" conditions for thin flyers would exist at the impact center. This heuristic prediction

⁶ D. A. Shockey, "Support of Armor Fragmentation Studies," SRI Project PYU 2151, 15 October 1973.

⁷ D. A. Shockey, "Hypervelocity Impact and Associated Phenomena," SRI Project PYU 2151, 18 December 1973.

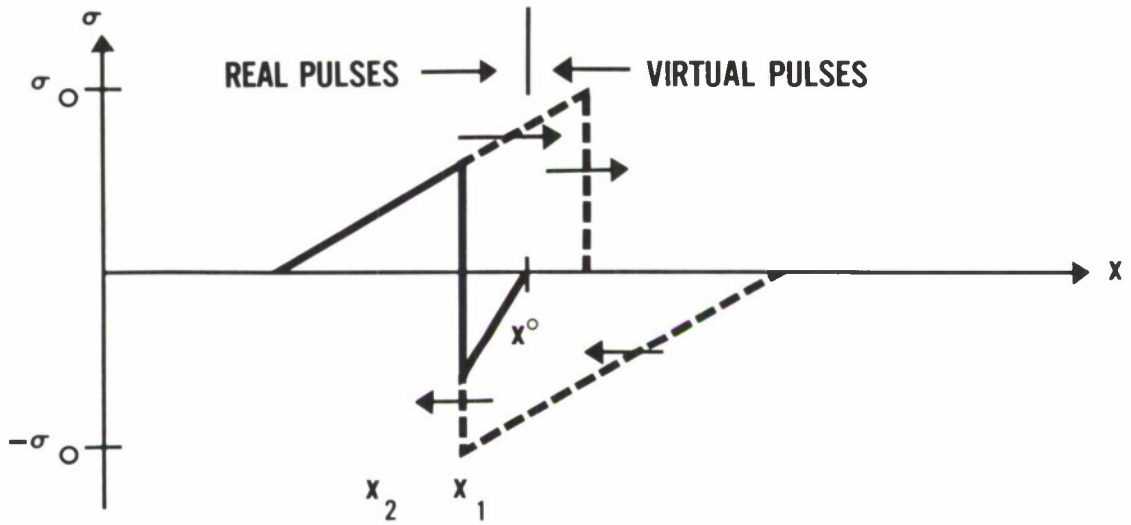


Figure 3. Spall layer formed by a triangular pulse.

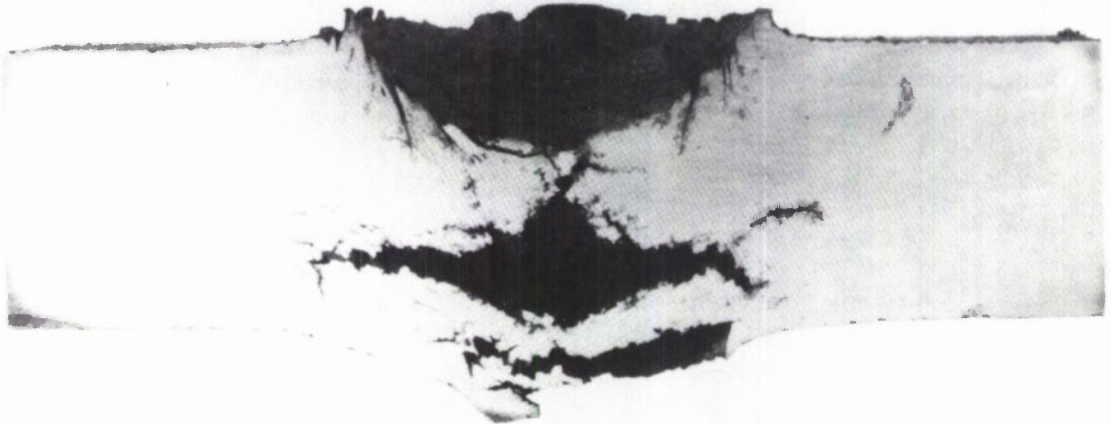


Figure 4. Spallation damage in 1.25-cm wrought steel by hollow Lexan sphere. Mass = 0.565 g; diameter = 1.08 g; impact velocity = 5.6 km/s.

was eminently borne out in several experiments in which the projectiles were hollow spheres. An example is shown in Figure 4. In this case the projectile was a hollow lexan sphere weighing 0.56 g with a diameter of 1.08 cm and an impact velocity of 5.59 km/s. Note the double spall layer and the backface fragmentation.

A few other impact experiments were performed in which the projectile was computer-designed to optimize backface spall. These experiments were particularly successful in showing that backface spall can be optimized.

III. DISCUSSION OF EXPERIMENTAL RESULTS

In general, a well-conceived experimental program produces results that have not been predicted theoretically. This program is no exception. The experimental "surprises" are too numerous to cover in this report; but a few of the more important results can be discussed:

1. Serrations on the crater floor for nylon- and water-steel impacts have not been explained. In particular, the reason for the serration formation on nylon-steel impact and the lack of serration formation on steel-steel impact have not been explained.

2. Preliminary or tentative explanation of the macrocracks observed for nylon-on-steel impacts has been given. But this explanation fails to show why the macrocracks extend upward for steel-steel impacts as compared to downward for nylon-on-steel impacts.

3. Shear lines are observed below the crater floor in almost all of the cases. Their role in the damage process has not been explained, however.

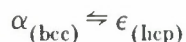
4. The macroscopic voids observed below the crater center have not been explained.

5. The importance of the observed 130-kbar phase change has been explained for one case. This is discussed in Section IV. Much more work is needed on this phenomenon.

6. Spallation: the 2-d computer calculations performed by SLA have shown excellent agreement with one impact experiment. This applies to the configuration and location of the spall layer for a relatively simple case. If this work could be extended to more important and relevant cases it would be of extreme significance.

7. General Summary.

a. **Metallographic/Fractographic Features.** As indicated previously, considerable circumstantial evidence leads to the conclusion that the dark-etching hemispherical volume of material under the impact site, such as shown in Figure 2, has undergone the pressure-induced phase transformation:



Material within this zone is of significantly finer grain structure and higher hardness than material elsewhere. Back surface laser interferometer records obtained in plate slap experiments by SLA exhibit clearly the disturbance attributable to a wave reflected from a denser (ϵ) phase.⁸

Profuse shear bonding was observed in the subcrater region and is felt to play an important role in the cratering process. The long cracks extending into the armor steel from the crater walls tend to lie on shear bands and tend to join with isolated pieces of material that form part of the ejecta.

Shear bands that are not associated with the crater walls are also prominent in the transformed region. A number of equiaxed microfractures having a ductile appearance are generally present in this region, linked together by shear bands, which are easily observable because of their distinct etching behavior. Again, cracks are observed to have formed in the bands and suggest the mechanism of material removal in this region. No evidence of shear was found in the back surface regions.

Fracture damage in the back surface region proceeds by the nucleation, growth, and coalescence of microfractures, followed by a widening of the resulting macrocrack and subsequent scabbing of the back surface by a shearing process that does not appear to be adiabatic. Observations of back surface damage at all stages of development were possible because of the wide variations in impact conditions. Detailed stress histories were not obtained, however.

b. **Correlations with Stress History.** An attempt was made to correlate metallographic and fractographic features observed in the specimens with stress histories. Only one impact experiment (described in Section IV of this report) was simulated computationally (by SLA). Many of the essential features of the stress history, however, may be similar in other experiments. Thus the following correlations may be common to hypervelocity impact in general (although many more experiments, metallurgical analyses, and theoretical extensions are needed before this statement can be properly delineated). The observed features for the single case described here were predicted (post-test) with outstanding accuracy by the SLA.

⁸ D. A. Shokey, "Hypervelocity Impact and Associated Phenomena," SRI Project PYU 2151, 18 December 1973.

(1) The boundary of the distinct etching region that had undergone the polymorphic phase transformation corresponds to a 130-kbar isobar. Furthermore, SLA showed that the effect of the phase transformation is to increase the stress pulse duration and, hence, the back surface damage. Thus, all other things being equal, an armor steel that does not exhibit this phase transformation (such as fcc steel) should be less subject to impact spallation damage than one that does.

(2) The ductile void-like microfractures in the subcrater region correlate qualitatively with the high triaxial tensile stresses and the elevated temperatures that exist there shortly after impact. Shock heating occurs as the compressive wave propagates through this region, driving the temperature up and relaxing the yield stress. Release waves run in from that part of the impact surface, not under the projectile, and intersect under the crater, creating a stress state having a large component of spherical tension. Microfractures begin to nucleate and grow, and the elevated temperatures favor the ductile void growth mode.

(3) The microhardness profiles are also in accord with the computed stress histories. A test profile made on the section surface in the direction of impact showed a high, reasonably constant level of hardness in the transformed zone that fell sharply to the original hardness at the boundary of the dark, or shaded, region. Profiles taken at 45° to the impact direction, however, exhibited a double humped behavior. The initial drop in hardness (within the transformed zone) detected by 45° profiles is attributed to release waves that run from the free impact surface into the subcrater regions and partially unload the material. The single humped profile in the impact direction is consistent with this being a line of symmetry.⁹

(4) Shear banding in the subcrater region is also consistent with the computed stress history, high shear stresses being predicted in the armor near the projectile-target interface. The shear bands connecting the subcrater voids are thought to form rather late in the event. The original spherical tensile field is distorted by the nucleation and growth of voids, which give rise to significant shear stresses. The shear stresses are relieved by plastic flow, which is concentrated in narrow bands running between the voids. The material within the bands gets very hot but is quenched immediately by the steel on either side. Therefore, this material transforms to austenite (fcc) and then quickly to martensite, which is hard and brittle, and acquires cracks under subsequent stress reverberations.

(5) The formation of spallation or fracture damage is perhaps the best understood feature observed in the impact specimens, as evidenced by the excellent agreement with the SLA predictions of damage morphology. The damage occurs by

⁹ D. A. Shockey, "Hypervelocity Impact and Associated Phenomena," SRI Project PYU 2151, 18 December 1973.

the nucleation, growth, and coalescence of microcracks when the compressive pulse reflects from the back surface and interacts with the release wave from the front surface. The formation and fragmentation of backface spall is not well understood, however.

(6) As a result of the effects and measurements discussed previously and the two-dimensional calculations discussed in Section IV, it is possible that the magnitude and duration of the tensile pulse calculated by the SLA 2-d codes can be used in conjunction with the material dynamic fracture parameters to predict the extent of back face fracture damage in quantitative microscopic detail. However, more quantitative correlations clearly require more experiments and more detailed 2-d computations, in addition to quantitative metallurgical examination of the specimens (counting, measuring, and positioning individual artifacts on the polished surfaces).

(7) Measurements show that at equal kinetic energies, spherical nylon projectiles are as effective as steel projectiles in producing back surface damage, and at equal momentum nylon projectiles are much more effective than steel projectiles. It is not clear at this time, however, which is the more important parameter—energy or momentum.

IV. 2-d COMPUTATIONS

It was fortuitous that the MERADCOM impact spallation experiments began about one year before SLA scheduled their new two-dimensional hydrodynamic codes for usage. Accordingly, in May 1973, SLA began to code the impact of a nylon sphere on 1.25-cm steel armor. The experimental results are shown in Figure 1. The impact velocity was 5.18 km/s and the projectile mass 0.52 g.

Two-dimensional code calculations of this test were performed at SLA using both the CSQ Eulerian Code and the TOODY Lagrangian Code with rezoning.¹⁰ The initial impact pressure was about 400 kbar, which causes iron and martensitic steel near the impact point to undergo the $\alpha \rightarrow \epsilon$ polymorphic phase change. The nylon sphere greatly distorts and goes into a liquid, partially vapor state. The steel plate suffers a large distortion near the impact point and requires both an accurate elastic-plastic model and a good material-failure model elsewhere in the plate. Also, a high degree of resolution is required for predicting complete or internal spallation because the attenuation of the initial compressive pulse, its reflection, and the interaction of the compressive and the reflected release wave must all be calculated accurately.

¹⁰ D. A. Shockey, "Hypervelocity Impact and Associated Phenomena," SRI Project PYU 2151, 18 December 1973.

The 130-kbar phase change, the correct spall strength, and an adequate failure model have all been determined to be important for predictive and interpretive calculations. A detailed examination of the stress histories for the cases with and without the phase change has shown why different failures should be expected in these two cases.¹¹ When the phase change is included in the calculations, the loading portion of the stress wave consists of two parts as the wave separates at 130 kbar. More important is the difference observed as unloading occurs; a rarefaction shock is present when the phase change is included. These differences in the stress wave structure not only cause a cylindrical-conical failure to occur directly below the crater but also to result in a propagating pulse that is nearly square for the case with a phase change and nearly triangular without. Upon reflection from a free surface, the square pulse transfers essentially all the momentum to the spall layer, whereas the triangular pulse is not nearly as effective in momentum transfer. This clearly shows the importance of the stress pulse shape in producing effective spall.

The measured spall stress of 38 kbar^{12 13} for the MS 12560 steel was used in the foregoing calculations, and the results showed excellent agreement with the experiment. This was especially true for the Lagrangian results where the crater diameter, crater depth, spall layer thickness, spall length, spall bulge, cylindrical-conical failure, and the area that undergoes a phase change all show nearly one-to-one correspondence with the experiments. The calculations did not reproduce the serrations in the crater floor, however, nor the macrocracks and shear bands observed below the crater floor.

When the phase change is included in both the CSQ and the TOODY calculations, the only significant difference is the spall length (or diameter). This difference is a direct result of the material failure treatment at the spall plane where a material coordinate treatment allows a higher accuracy. The very good numerical and experimental agreement demonstrates the capability of the codes to solve a wide class of difficult and important problems, although much more correlation between calculations and experiments is needed.

V. THE 130-kbar PHASE CHANGE IN MARTENSITIC STEEL

In recent years, a number of measurements have been made of the high-pressure properties of iron in the regions of the $\alpha \rightarrow \epsilon$ phase transition. These indicate that at room temperature the transition occurs in the region of 130 kbar and that it is abaric, initiating at about 130 kbar and going to completion at pressures > 170 kbar. The observed specific volume change associated with the transition is $\Delta V \cong 0.0066 \text{ cm}^3/\text{g}$

¹¹ D. A. Shockey, "Hypervelocity Impact and Associated Phenomena," SRI Project PYU 2151, 18 December 1973.

¹² A. Stevens, Personal Communication, SLA, 1973.

¹³ D. A. Shockey, "Hypervelocity Impact and Associated Phenomena," SRI Project PYU 2151, 18 December 1973.

and the compression ratio at the onset of the transition is $x \cong 0.943$. Here, x is the specific volume, v , divided by the specific volume, v_0 , of α -Fe at 0° K and zero pressure.¹⁴

The phase diagram of Fe is shown in Figure 5. According to the SLA calculations, the shock temperature in the Fe does not go high enough to drive the steel into the α phase. The shock pressure does get high enough, however, to drive the steel into the ϵ phase from which it reverts, on cooling, to the α phase, with a consequent change in grain structure and mechanical properties. Direct active measurements to show this change have not been made, but a combination of theory, computations, and metallurgical analysis indicates that this history is correct.

Mossbauer measurements¹⁵ show that the magnetic momentum per atom μ is practically constant for the α phase up to the pressure of its disappearance and that the ϵ phase is non-ferromagnetic. These measurements also imply that the number N_s of s-electrons per atom is invariant with pressure for the α phase; whereas, for the ϵ phase, N_s decreases with increasing pressure.

Upon the reduction of pressure, the ϵ phase persists down to a pressure of about 45 kbar, causing hysteresis in the compressional behavior of iron in the vicinity of the transition. At pressures below 45 kbar, the ϵ phase disappears completely. Recent dynamic measurements, using shock waves, have been made.¹⁶ These confirm the non-ferromagnetic nature of the ϵ phase and, in addition, show some demagnetization (an apparent reduction of μ) at pressures as low as 50 kbar.

The response of a metal to dynamic loading depends upon three elements which are characteristic of the material: the dynamic constitutive relation, the pressure-temperature phase relation, and the dynamic fracture criteria. In the absence of phase changes or fracture, the material response is governed completely by the constitutive relation, or dynamic equation of state. The constitutive relation is characterized as "elastic," "viscoelastic," "viscoelastic-plastic," etc. It depends on macroscopic parameters such as Young's modulus and the viscosity coefficient which, on a microscopic scale, arise from atomic interactions and dislocation processes.

The phase diagram determines whether a given loading history will bring the metal into a pressure-temperature regime where phase transitions are possible. If this occurs during shock loading, multiple shock waves may result.

¹⁴ D. J. Andrews, "Equation of State of the Alpha and Epsilon Phases of Iron," Washington State University, WSU SDL 70-05, November 1970.

¹⁵ *Ibid.*

¹⁶ D. J. Pastine, "A Theory of the $\alpha \rightarrow \epsilon$ Transition in Fe and of Possible Higher Pressure Transitions in Fe and in the Lighter Elements of the First Transition Series," NOL, in *Metallurgical Effects at High Strain Rates*, Plenum Press, 1973.

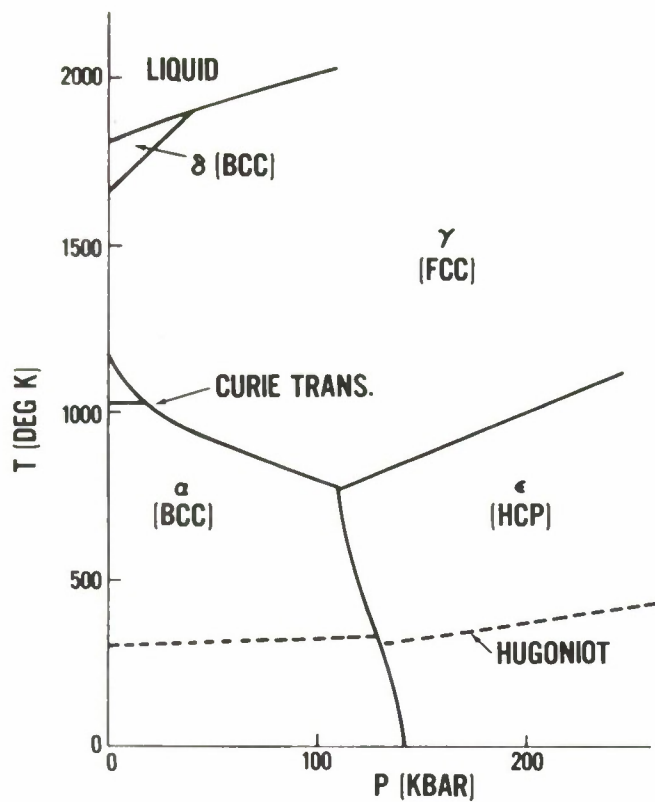


Figure 5. Phase diagram of iron.

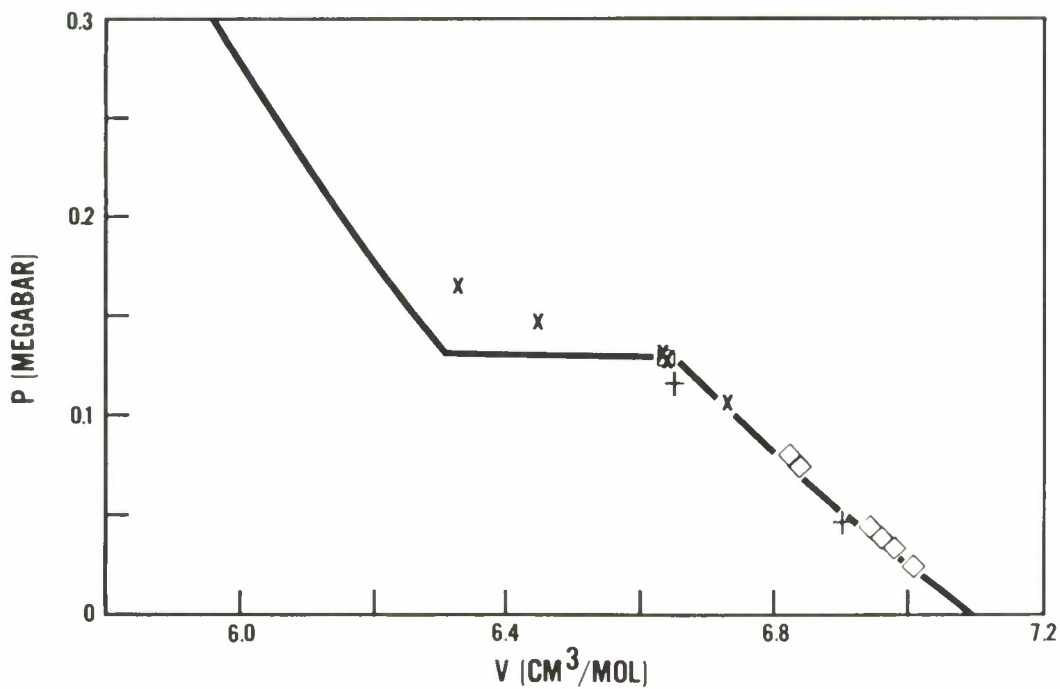


Figure 6. Hugoniot states of iron.

In macroscopic or rheological language, iron can be described as a viscoelastic-plastic material; i.e., it responds elastically until yielding (with upper and lower yield points) and is strongly rate-dependent. The constitutive relation thus gives the stress as a function of strain and time or, alternatively, can be written as a differential equation in σ , ϵ , $\dot{\sigma}$, and $\dot{\epsilon}$. An important goal of present-day research is to develop the capability to derive this macroscopic constitutive relation by averaging the effects of microscopic processes. In iron, the density of mobile dislocations is of the order of $10^8/\text{cm}^2$, which is large enough to make a statistical approach valid.

The dynamic response of iron to shock loading at relatively low stress levels is fairly well understood on the basis of a dynamic constitutive relation that is derived from average dislocation properties. However, it is not yet possible uniquely to derive the constitutive relation from dislocation properties because the correct dislocation model based on statistical averaging of dislocation processes has not been completely determined. Nevertheless, it is to be expected that dynamic experiments selected to distinguish between different dislocation models, and growing understanding of the dislocation mechanisms themselves, will eventually fill in most of the remaining gaps.

As noted above, a complicating factor in the dynamic response of iron to shock loading is the presence of pressure-induced phase changes. This has been discussed briefly before. In order to determine whether a given loading history will cause a phase change, the high-pressure phase diagram of iron must be known. The pressure-induced phase changes in iron have many formal similarities to plastic yielding. Put another way, the elastic-plastic transition with strain hardening can be regarded as a second-order phase change, since it involves no discontinuity in the stress-strain curve but does involve discontinuities in the gradients. The kinetics of plasticity rest on activation and multiplication of dislocations, and the kinetics of a crystallographic phase transition are based on the similar but more extensive atomic motions which change the crystal structure locally. Thus, the constitutive relations can, in principle, account for phase changes in a manner analogous to the way they handle plasticity.

At about 130 kbar, α iron begins a transformation to a form which is about 3 percent denser. As shown in Figure 5, three crystallographic phases of iron are found to be stable in different regions of the pressure-temperature plane. The triple point is at about 115 kbar and 775 K.

The P-T path corresponding to high-velocity impact loading of iron initially at room temperature will intersect the α - ϵ coexistence curve at a point corresponding to about 130 kbar. The effect of the volume compression during the phase change will cause a shock wave of initial strength between 130 and 330 kbar to split into two shock waves traveling at different velocities. Upon reflection from free surfaces, the compressive shock waves are transformed to unloading waves which may intersect to

produce a tensile stress history that causes damage and failure.¹⁷ The presence of the $\alpha \rightleftharpoons \epsilon$ phase change can result in extremely steep unloading waves or "rarefaction shocks," which are effective in causing fracture. The regime in the P-T plane reached during loading is dependent, of course, on the temperature of the iron prior to unloading and on whether the iron is stressed and heated simultaneously during loading.

VI. INCIPIENT SPALL OR FRACTURE CRITERIA

Dynamic fracture criteria for incipient spall have been considered in great detail by various authors.¹⁸ This is discussed here briefly. Complete spall and backface fragmentation are discussed in Section VII.

In the case of quasi-static loading of brittle materials, it is often possible to apply a simple fracture criterion; namely, that a critical tensile stress exists beyond which failure occurs. Sample geometry and the effects of elastic material properties and initial crack size can be included by determining the fracture toughness, which is related to the maximum stress concentration at a crack tip allowable before an initially present crack propagates.

This simple criterion is not compatible with the results from dynamic experiments, however, since it is found that there is a time dependence for dynamic failure; i.e., the fracture criterion depends on the entire stress history. For square pulses, this time dependence of dynamic fracture has been shown to be consistent with a relationship between tensile stress and the time duration of tensile stress, Δt . This relationship is

$$(\sigma - \sigma_o)^\lambda \Delta t = K$$

where σ_o , λ , and K are constants specific to a particular material. If $\lambda = 1$, this is a simple impulse criterion. With $\lambda = 2$, it is equivalent to an energy criterion. With $\lambda = 1$, the equation can also be related to other time-dependent fracture criteria, such as stress-gradient and stress-loading rate, which are consistent with data resulting from explosive tests. These criteria are based primarily on a simple classification of damage into categories of no damage, damage, and failure. What is needed is a model which relates fracture behavior to detailed observations of the damage resulting from a given stress history. Such correlations are necessary for interpretation of the effects of material properties on dynamic failure and to ensure that realistic models for dynamic fracture are investigated.¹⁹

¹⁷ D. R. Curran, "Dynamic Mechanical Behavior of Iron," in *Shock Waves and the Mechanical Properties of Solids* (ed. J. J. Burke and V. Weiss), Syracuse Union Press, 1971.

¹⁸ *Ibid.*

¹⁹ *Ibid.*

Another approach is based on treating damage as a new phase of the material, where the nucleation and growth of the new phase, damage, can be correlated with *macroscopic* stress history and *microscopic* material properties. In other words, just as phase changes can be treated in a manner analogous to the growth of plasticity, the appearance of damage can also be treated in this way. A necessary condition is that the number of microcracks be sufficiently large to make a statistical approach valid. The steps of the method are: (1) shock and recover specimens; (2) describe the size and spatial distribution of the cracks quantitatively; (3) achieve experimental control so that the cracks can be stopped in different stages of growth; and (4) specify the microscopic stress and times-at-stress experienced at any location in the specimen. If the stress history is sufficiently uncomplicated, then it is possible to correlate the observed damage to the stress history of the specimen in such a way that nucleation and growth laws of general validity may be derived. Once these factors are known, quantitative predictions can be made of damage caused by an imposed stress history.

This approach has the significant advantage of bypassing the difficult problem of calculating stress distributions around microcracks. Instead, the large number of microcracks present allows a statistical approach, and the crack number distribution functions can be correlated with microscopic stress histories. In many ways, this is analogous to the derivation of constitutive relations from average dislocation processes. The large number of dislocations present made it possible to use a statistical approach and thus avoid the problem of calculating microscopic stress fields around individual dislocations.

VII. COMPLETE AND BACKFACE SPALL

As discussed in Section VI, microcracks and voids begin to form when the tensile stress reaches the "spall threshold" or the incipient spall strength. For practical purposes, a certain microcrack size or density is assigned to this value.

As the tensile stress exceeds the spall threshold, the microcracks begin to coalesce until a complete spall layer is formed. For the impact experiments with spherical projectiles described in this report, the surface of the spall layer nearest the backface is generally parallel to the backface of the target at a distance d from the backface. For a given type of projectile d is constant over the velocity range from 3 to 7 km/s. The spall layer has a thickness δ (perpendicular to the backface), which increases rapidly with velocity above the incipient threshold. In addition to the spall layer thickness, there is a backface bulge with height h , which is equal to δ . As long as the spall layer is formed near the backface, h is a useful experimental (or empirical) parameter since it can be measured with good accuracy, whereas measurements of δ are sometimes ambiguous. The spall layer has a diameter D (parallel to the backface) that increases slightly with impact velocity. It grows to be somewhat greater than the crater

diameter (parallel to and at the target surface). At some high impact velocity the backface "plugs," or fragments; i.e., material of thickness d and (approximate) diameter D is ejected from the backface either as a single plug or as a number of smaller fragments. The impact velocity to produce incipient spall is V_o and for backface spall, it is V_{∞} . As will be seen, V_{∞} appears to be about twice V_o for the experiments described.

Backface bulge height h is plotted on linear paper as a function of impact velocity for three different cases in Figure 7. It is seen that the experimental points lie reasonably well on smooth curves. The points have been plotted for the 0.52-g nylon sphere on the 1.25-cm steel target on semilog paper in Figure 8. The points fall well on a straight line, which suggests that the fractional increase in h (or δ) increases with incremental velocity; i.e.,

$$\Delta h = k \delta \Delta V$$

where k is a constant. Upon integration this becomes

$$h = h_o e^{k(V-V_o)}$$

For the purposes here, h_o can be assumed to correspond to the bulge height at incipient spall, with V_o the corresponding impact velocity. Empirical values for k and V_o are given in the following table for the three cases shown in Figure 7.

Projectile Material	Projectile Mass (g)	Target Thickness (cm)	h_o (cm)	k (s/km)	V_o (km/s)
Nylon	0.52	1.25	0.01	1.55	2.77
Nylon	1.01	2.5	0.01	1.40	3.85
H ₂ O/Lexan	0.35	1.25	0.01	1.43	3.23

Admittedly, while much more experimentation, analysis, and theory are needed, it appears that the above results may provide a good working criterion for complete spall and, possibly, for backface spall. This is important for the systems engineer who is concerned about evaluating certain types of military systems at minimum cost. If the hypotheses reported here are true, it means that one impact experiment chosen for a given target, a given projectile, and over the hypervelocity range may be sufficient to obtain values for both incipient spallation and backface spall.

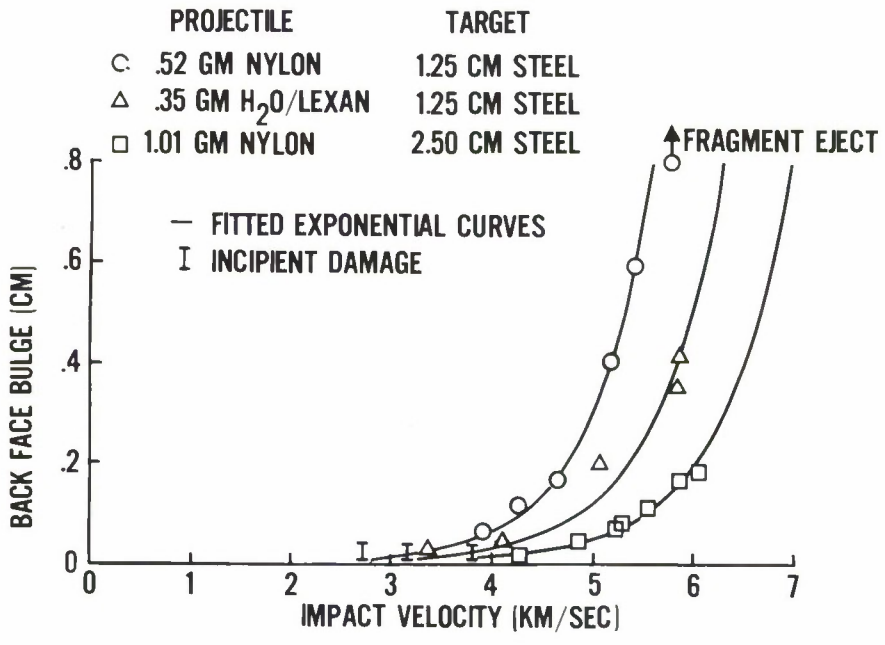


Figure 7. Spall damage in homogeneous wrought steel plate.

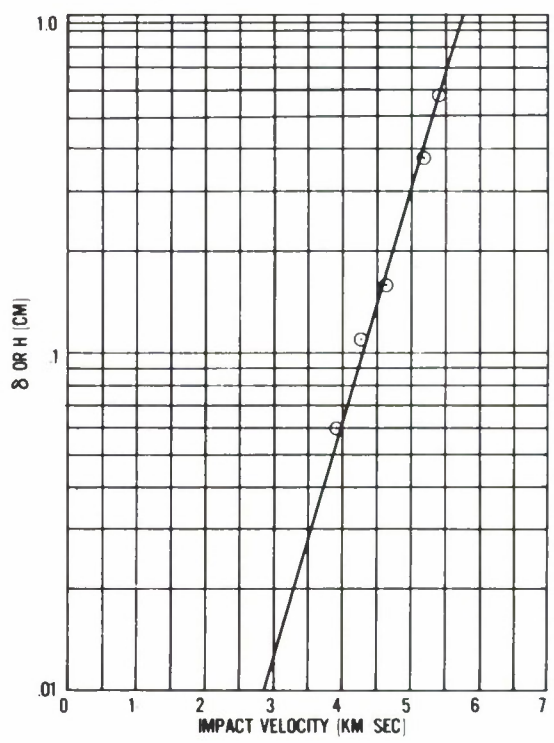


Figure 8. Backface bulge (or spall layer thickness) vs. impact velocity.

At present, 2-d computations are not sufficiently reliable to provide the necessary predictions; in any event, they are prohibitively expensive. Furthermore, a series of impact experiments, such as those shown in Figure 7, is also expensive. On the other hand, one shot of the sort described is relatively inexpensive.

In order to justify the reported hypotheses, correlation between the assumption that $h_0 = 0.01$ cm and the value of h corresponding to the definitions of incipient spall given in Section VI is needed. Based on experimental results and analysis, it is felt that such a practical correlation can be obtained.

The value for V_{∞} is a different matter. Even heuristic theory capable of predicting V_{∞} is not available, although relevant experiments are planned. It was indicated previously that $H_2O/Lexan$ and nylon spheres are somewhat comparable for producing impact-induced spallation. It is seen from Figure 7 that, for a given target and for plastic and liquid spherical projectiles, V_{∞} varies inversely as the projectile mass. The relation between target thickness and projectile characteristics is not clear, although some crude empirical formulas may be possible.

VIII. SUMMARY AND CONCLUSIONS

The results of extensive hypervelocity impact experimentation on martensitic steel armor have been summarized. It has been suggested that certain types of austenitic steel may be less subject to spallation damage than martensitic steel. Damage criteria from complete and backface spall have been discussed, and heuristic or empirical theory for predicting backface spall in martensitic steel armor has been suggested. The main conclusion of this work is that the $\alpha - \epsilon$ phase change for martensitic steel is important in predicting or interpreting projectile impact damage. Other conclusions are more general and possibly not applicable for present purposes. For example, a preliminary conclusion is that hypervelocity-impact-induced backface spall is a viable damage mechanism. Another preliminary conclusion is that efficient spallators capable of optimizing backface spall are feasible. The main conclusion is that more experiment, theory, analysis, and computations are needed.

DISTRIBUTION FOR MERADCOM REPORT 2174

No. Copies	Addressee	No. Copies	Addressee
	Department of Defense	1	Commander, HQ TRADOC ATTN: ATEN-ME Fort Monroe, VA 23651
1	Director, Technical Information Defense Advanced Research Projects Agency 1400 Wilson Blvd Arlington, VA 22209	1	HQDA (DAMA-AOA-M) Washington, DC 20310
1	Director Defense Nuclear Agency ATTN: STTL Washington, DC 20305	1	HQDA (DALO-TS M-P) Washington, DC 20310
12	Defense Documentation Center Cameron Station Alexandria, VA 22314	1	HQDA (DAEN-RDL) Washington, DC 20314
1	Director Defense Nuclear Agency ATTN: Mr. Jim Moulton Washington, DC 20305	1	Commander US Army Missile Research & Development Command ATTN: DRSMH-RR Redstone Arsenal, AL 35809
1	Director of Defense, Research & Engineering (OSD) ATTN: Mr. J. Persh Washington, DC 20301	1	Chief, Engineer Division DCSLOG ATTN: AFKC-LG-E HQ Sixth US Army Presidio of San Francisco, CA 94129
1	Director of Defense Research & Engineering (OSD) ATTN: Mr. G. R. Makepeace Washington, DC 20301	1	Director Army Materials and Mechanics Research Center ATTN: DRXMR-STL Technical Library Watertown, MA 02172
3	Director Defense Advanced Research Projects Agency ATTN: Dr. Ernie Blase Dr. Robert Moore Dr. Heilmyer 1400 Wilson Blvd Arlington, VA 22309	1	US Army Ballistic Research Laboratories Technical Library DRXBR-LB (Bldg 305) Aberdeen Proving Ground, MD 21005
	Department of the Army		
6	Commander US Army Materiel Development & Readiness Command ATTN: DRCRD-WB DRCRD-T DRCRD-J DRCRD-O DRCRD-G DRCRD-FP 5001 Eisenhower Ave Alexandria, VA 22333	1	Commander Edgewood Arsenal ATTN: SAREA-TS-L Aberdeen Proving Ground, MD 21010
		1	Commander US Army Aberdeen Proving Ground ATTN: STEAP-MT-U (GE Branch) Aberdeen Proving Ground, MD 21005

No. Copies	Addressee	No. Copies	Addressee
1	Director US Army Materiel Systems Analysis Agency ATTN: DRXSY-CM Aberdeen Proving Ground, MD 21005	1	Commander Special Forces Detachment (Airborne), Europe APO New York 09050
1	Director US Army Engineer Waterways Experiment Station ATTN: Chief, Library Branch Technical Information Center Vicksburg, MS 39180	1	HQ, USAREUR & Seventh Army DCSENGR ATTN: AEAEN-MO ATTN: Mil Ops Div APO New York 09403
1	Commander Picatinny Arsenal ATTN: SARPA-TS-S No. 59 Dover, NJ 07801	2	Engineer Representative US Army Standardization Group, UK Box 65, FPO New York 09510
1	Commander US Army Troop Support & Aviation Materiel Readiness Command ATTN: DRSTS-KTE 4300 Goodfellow Blvd St Louis, MO 63120	1	Commander Rock Island Arsenal ATTN: SARRI-LPL Rock Island, IL 61201
2	Director Petrol & Fld Sve Dept US Army Quartermaster School Fort Lee, VA 23801	1	Plastics Technical Evaluation Center Picatinny Arsenal, Bldg 176 ATTN: A. M. Anzalone SARPA-FR-M-D Dover, NJ 07801
1	Commander US Army Electronics Research & Development Command ATTN: DRSEL-GG-TD Fort Monmouth, NJ 07703	1	Commander Frankford Arsenal ATTN: Library, K2400, B1 51-2 Philadelphia, PA 19137
1	President US Army Aviation Test Board ATTN: STEBG-PO Fort Rucker, AL 36360	1	Learning Resources Center US Army Engineer School Bldg 270 Fort Belvoir, VA 22060
1	US Army Aviation School Library P.O. Drawer 0 Fort Rucker, AL 36360	1	President US Army Airborne, Communications & Electronics ATTN: STEBF-ABTD Fort Bragg, NC 28307
1	HQ, 193D Infantry Brigade (CZ) Directorate of Facilities Engineering Fort Amador, Canal Zone	1	Commander Headquarters, 39th Engineer Battalion (Cbt) Fort Devens, MA 01433
		1	President US Army Armor and Engineer Board ATTN: ATZK-AE-TD-E Fort Knox, KY 40121

No. Copies	Addressee	No. Copies	Addressee
1	Commandant US Army Command and General Staff College ATTN: ATSW-RI-L Fort Leavenworth, KS 66027	1	Director Ballistics Research Laboratory ATTN: Dr. John Frazier Aberdeen Proving Ground, MD 21005
1	Commander 2nd Engineer Group ATTN: S4 APO San Francisco 96301	1	Technical Director MICOM ATTN: Dr. Post Hallowes Dir Phys Sci Directorate Redstone Arsenal, AL 35809
1	Commander and Director USAFESA ATTN: FESA-RTD Fort Belvoir, VA 22060	3	Commander Picatinny Arsenal ATTN: Mr. Sidney Jacobson SARPA-AD-D-2 Mr. William Painter Tech Dir Mr. J. Pearson Dover, NJ 07801
1	Dr. Malcolm Curry ODDR&E The Pentagon Washington, DC 20305	1	Assistant Secretary of the Army (R&D) ATTN: Dr. K. C. Emerson Assistant for Research Washington, DC 21310
1	Director Army Material Systems Analysis Agency ATTN: M. Smith Aberdeen Proving Ground, MD 21005	1	Headquarters Dept of the Army ATTN: Mr. David Hardison Adv for RDA Analysis Rm. 3E411 Pentagon Washington, DC 20310
3	Commander US Army Armaments Command ATTN: J. A. Brinkman, Tech Dir Dr. Richard Moore W. Wohlford Rock Island Arsenal, IL 61201	1	HQDA (DARD-ARZ-B Dr. I. R. (Hershner) Washington, DC 20310
1	HQDA (DARD-ARP-E, Dr. J. Bryant) Washington, DC 21310	1	USA Mobility Equipment Research & Development Command ATTN: DRXFB-VM (Mr. Howard E. Horner) Fort Belvoir, VA 22060
1	Director Ballistics Research Laboratory ATTN: Dr. Robert Eichelberger Tech Dir Aberdeen Proving Ground, MD 21005	1	Dr. John C. Hurt USA Research Office P.O. Box 12211 Research Triangle Park, NC 27709
1	Clint Frank Ballistics Research Laboratory Aberdeen Proving Ground, MD 21005	1	US Army ABMDA ATTN: Leonard I. Kopeikin Commonwealth Bldg 1320 Wilson Ave Arlington, VA 22209
1	Director Ballistics Research Laboratory ATTN: Dr. William Gillich Aberdeen Proving Ground, MD 21005		

No. Copies	Addressee	No. Copies	Addressee
1	USA Natick Research & Development Command ATTN: DRXNM-VTF (Mr. Roy C. Laible) Kansas Street Natick, MA 01760	1	Commander US Army Training and Doctrine Command ATTN: Dr. M. Pastel, ATCD-SI Fort Monroe, VA 23651
1	HQDA (DARD-ZC Dr. M. E. Lasser) Washington, DC 20310	1	US Army Tank Autom. Dev Com ATTN: AMDTA-RK (Victor Pagano) Warren, MI 48090
1	Charles Lehner Advanced Research Projects Agency 1400 Wilson Blvd Arlington, VA 22209	1	Dr. Hermann Robl USA Research Office P.O. Box 12211 Research Triangle Park, NC 27709
1	Ballistics Research Laboratories ATTN: Dr. Gerry Moss Aberdeen Proving Ground, MD 21005	1	Ballistics Research Laboratory ATTN: Dr. Harry Reed Aberdeen Proving Ground, MD 21005
1	Mr. Cliff McClam Ballistic Missile Defense Agency 1300 Wilson Blvd Arlington, VA 22209	1	Ballistics Research Laboratories ATTN: Dr. Richard Vitali Aberdeen Proving Ground, MD 21005
2	Director US Army Mechanics and Materials Research Agency ATTN: J. Mescall Dr. Ed Wright, Assoc Dir Watertown, MA 02172	1	Director of Defense Research & Engineering (OSD) ATTN: Mr. R. Thorkildsen Washington, DC 20301
1	COL Lothrop Mittenthal USA Research Office P.O. Box 12211 Research Triangle Park, NC 27709	1	Director US Army Materiel Systems Analysis Agency ATTN: AMXSY-D Dr. J. Sperrazza Aberdeen Proving Ground, MD 21005
1	US Army Armaments Command ATTN: AMSWE-RDR Dr. Richard Moore Rock Island Arsenal, IL 61201	1	Dr. Edward A. Saibel USA Research Office P.O. Box 12211 Research Triangle Park, NC 27709
2	US Army Research Office ATTN: Dr. James Murray Dr. George Mayer Box 12211, Research Triangle Durham, NC 27709	1	Dr. Dilip Shah SARRI-LR-4833 Rock Island Arsenal Rock Island, IL 61201
1	Ballistics Research Laboratories ATTN: Paul Netherwood Aberdeen Proving Ground, MD 21003	1	HQDA (DARD-DDZ-P Dr. R. B. Watson) Washington, DC 21310

No. Copies	Addressee	No. Copies	Addressee
1	Dr. Robert Weigel ARDC Provisional Headquarters DRCSA-RP Building 3002 Picatunny Arseual Dover, NJ 07801	1	Commander, Naval Facilities Engineering Command Department of the Navy ATTN: Code 032-A 200 Stovall St Alexandria, VA 22332
1	Col. Wm. Whitaker DARPA 1400 Wilson Blvd Arlington, VA 22209	1	US Naval Oceanographic Office Library (Code 1600) Washington, DC 20373
	MERADCOM	1	Officer-in-Charge (Code L31) Civil Engineering Laboratory Naval Construction Battalion Center Port Hueneme, CA 93043
1	Commander Technical Director Assoc Tech Dir/R&D Assoc Tech Dir/Engrg & Aeq Assoc Tech Dir/Matl Asmt Assoc Tech Dir/Tech Asmt CIRCULATE	1	Director Earth Physics Program Code 463 Office of Naval Research Arlington, VA 22217
1	Chief, Lab 1000 Chief, Lab 2000 Chief, Lab 3000 Chief, Lab 4000 Chief, Lab 5000 Chief, Lab 6000 Chief, Lab 8000 Chief, Lab 9000 Chief, TARSO CIRCULATE	3	Commander Naval Research Laboratories ATTN: Walter Atkins Mario Persechino Tech Director Waslungton, DC 20332
3	Lab 7000	2	Commander US Naval Weapons Center ATTN: Mr. Backman Dr. John Pearson China Lake, CA 93555
30	Special Projects Div (Dr. J. W. Bond)	1	Commander Naval Surface Weapons Center ATTN: Dr. Arnold Siegel White Oaks, MD 20910
3	Tech Reports Ofc		
3	Security Ofc		
2	Tech Library		
1	Requirements & Programs Ofc		
1	Information Ofc		
1	Legal Ofc	1	Dr. Jack Goeller Naval Surface Weapons Center/ WOL Code 322 Silver Spring, MD 20910
	Department of the Navy	1	Commander US Naval Surface Weapons Center ATTN: Dr. R. E. Wilson Silver Spring, MD 20410
1	Director, Physics Program (421) Office of Naval Research Arlington, VA 22217		
1	Director Naval Research Laboratory ATTN: Code 2627 Washington, DC 20375		

No. Copies	Addressee	No. Copies	Addressee
	Department of the Air Force	1	Professor Jan D. Achenbach Department of Civil Engineering Technological Institute Northwestern University Evanston, IL 60201
1	HQ USAF/RDPS (Mr. Allan Eaffy) Washington, DC 20330		
1	Mr. William J. Engle Chief, Utilities Branch HQ USAF/PREEU Washington, DC 20332	1	Professor Carl Altstetter 302 MMB Department of Metallurgy & Mining Engineering College of Engineering University of Illinois at Urbana-Champaign Urbana, IL 61801
1	AFSC/INJ Andrews AFB, MD 20334		
1	OL-AA AFCEC/DEZ Kirtland AFB, NM 87117	1	Professor A. S. Argon Room 1-312 Massachusetts Institute of Technology Cambridge, MA 02139
1	AFCEC/XR/21 Tyndall AFB, FL 32401		
1	HQ USAF/PREES ATTN: Mr. Edwin B. Mixon Bolling AFB-Bldg 626 Washington, DC 20332	1	Mr. Charles A. Anderson President Stanford Research Institute Menlo Park, CA 94025
1	AFAPL/SFL Wright-Patterson AFB, OH 45433	2	Battelle Columbus Laboratories ATTN: Dr. Dale Trott Stan Goddard 505 King Ave Columbus, OH 43201
1	ASD/ENCSP Wright-Patterson AFB, OH 45433		
1	Department of Transportation Library, FOB 10A, TAD-494.6 800 Independence Ave., SW Washington, DC 20591	2	Aerospace Corp ATTN: Mr. Thor Bergstrahl Dr. Sidney Kash El Segundo, CA 90245
1	AFATL (DLB, Dr. B. A. Kulp) Eglin AFB, FL 32542	1	Dr. R. S. Carbonara Battelle Columbus Laboratories Durham Office Durham, NC 27707
1	MG Jospser A. Welch, Jr. Ass't C/S, Studies & Analyses HQ USAF/SA Pentagon Washington, DC 20330	1	Professor R. J. Clifton Division of Engineering Brown University Providence, RI 02912
	Others		
1	Professor Raymond R. Fox School of Engineering and Applied Science The George Washington University Washington, DC 20052	1	Dr. D. R. Curran Stanford Research Institute Menlo Park, CA 94025
		1	Professor Keith Brnoshner Physics Dept Union of Calif at San Diego San Diego, CA 92109

No. Copies	Addressee	No. Copies	Addressee
1	Dr. John Batch Director Battelle Columbus Laboratories 505 King Avenue Columbus, OH 43201	1	Dr. James Lankford Southwest Research Institute P.O. Drawer 28510 San Antonio, TX 78284
1	Professor Ian M. Fyfe FS-10 Department of Aeronautics & Astronautics University of Washington Seattle, WA 98195	1	Mr. W. C. Lau Room 1-312 Massachusetts Institute of Technology Cambridge, MA 02139
1	Steven Gill ARTEC Associates, Mc 26046 Eden Landing Road Hayward, CA 94545	1	Professor J. C. M. Li Department of Mechanical & Aerospace Sciences University of Rochester Rochester, NY 14627
1	Charles S. Godfrey Physics International Co 2700 Merced Street San Leandro, CA 94577	1	Professor Hao-Wen Liu 409 Link Hall Syracuse University Syracuse, NY 13210
1	Professor J. Duffy Division of Engineering Brown University Providence, RI 02912	1	Professor L. E. Malvern Engineering Sciences Department 231 Aero Bldg University of Florida Gainesville, FL 32611
1	Professor Victor A. Greenhut College of Engineering Rutgers University New Brunswick, NJ 08903	1	Professor Donald E. Mikkola Department of Metallurgical Engineering Michigan Technological University Houghton, MI 49931
1	Dr. David W. Hoepfner University of Missouri-Columbia College of Engineering, Rm. 2007 Columbia, MO 65201	1	Professor Osear Orringer Department of Aeronautics & Astronautics Massachusetts Institute of Technology Cambridge, MA 02139
1	Professor Ray Kinslow Box 5002 Tennessee Technological University Cookeville, TN 38501	1	Dr. A. Narath Vice President, Research Organization 5000 Sandia Laboratories Albuquerque, NM 87115
1	Professor George Krauss Department of Metallurgical Engineering Colorado School of Mines Golden, CO 80401	1	Professor Arthur Paskin Queens College of the City University of New York Flushing, NY 11367
1	Professor Campbell Laird Department of Metallurgy & Materials Sciences University of Pennsylvania Bldg K1 Philadelphia, PA 19174		

No. Copies	Addressee	No. Copies	Addressee
1	Professor J. N. Reddy The University of Oklahoma 865 Asp Avenue Room 200 Norman, OK 73069	1	Professor Volker Weiss Conference Secretariat, ICM-II American Society for Metals Metals Park, OH 44073
1	Professor Harry C. Rogers Department of Materials Engineering Drexel University Philadelphia, PA 19104	3	Lawrence Livermore Laboratory ATTN: Tech Director Mark Wilkins Dr. Edward Teller Livermore, CA 94550
2	R&D Associates ATTN: Dr. Albert Latter Dr. Marvin Schafer P.O. Box 3580 525 Wilshire Blvd Santa Monica, CA 90403	1	Professor John Williams School of Engineering The University of Connecticut Storrs, CT 06268
1	Professor Martin Sommerfield University of Princeton Princeton, NJ 08540	1	Professor Kenneth Watson Physics Dept University of California Berkeley, CA 94720
1	Paul Tamarkin Rand Corporation Santa Monica, CA 90406		
1	Professor Dale F. Stein Department of Metallurgical Engineering Michigan Technological University Houghton, MI 49931		
1	Professor Robert Stilker Department of Aeronautics & Astronautics Massachusetts Institute of Technology Cambridge, MA 02139		
1	Professor T. C. T. Ting Department of Materials Engineering University of Illinois at Chicago Circle Chicago, IL 60680		
1	K. D. Seifert Physics International Co 2700 Merced Street San Leandro, CA 94577		